

EVALUATING THE LAMINAR FLOW ON A SLOTTED, NATURAL-LAMINAR-FLOW WING IN THE NASA AMES 11-FOOT TRANSONIC WIND TUNNEL

Koen J. Groot[1], Nick J. Porfido[2], Helen L. Reed[2], James G. Coder[3] & Dan M. Somers[4]

[1]University of Wyoming, Laramie, WY, 82070
[2]Texas A&M University, College Station, TX, 77843
[3]Penn State University, University Park, PA, 16802
[4]Airfoils, Incorporated, Port Matilda, PA, 16870

Abstract

In this article, the overarching objective is to confirm and evaluate laminar flow over the suction side of the fore element of a swept, slotted, natural-laminar-flow (SNLF) wing at full-scale transonic conditions in the NASA Ames 11-Foot Transonic Wind Tunnel (11-FT TWT). Toward this end, two technical contributions are implemented. First, a methodology is presented to extract the laminar-to-turbulent transition-region location from infrared thermography data on a frame-by-frame basis, including the masking of measurement artifacts and a Hough-transform-based algorithm to fit the upstream and downstream extents of the transition region and quantify its temporal uncertainty. Second, the measured surface pressure distributions are used to drive a compressible boundary-layer solver and Linear Parabolized Stability Equation (LPSE) computations, producing Tollmien-Schlichting (TS) N-factor isocontours that are compared directly against the measured transition locations. At the reference condition of $M = 0.7$ and $Re_c = 13 \times 10^6$ (based on the leading-edge-orthogonal chord), laminar flow is achieved over practically the entire suction side of the fore element for angles of attack between -1° and 0°, with transition conservatively bounded below by $N = 4$–5 for this facility. The N-factor at which transition occurs increases as the transition front moves upstream with increasing angle of attack, a trend that deserves further investigation. The N-factor isocontours furthermore become nearly vertical in the x/c–AoA plane across the rooftop region of the fore element, implying a high sensitivity of the transition location to small changes in angle of attack when the critical N-factor is reached. The laminar flow region expands as the Reynolds number is reduced, driven by the stronger favorable pressure gradient arising from the thickened boundary-layer displacement thickness, and as the Mach number is increased, driven by both the inherent compressible stabilization of the TS mechanism and the more favorable pressure distribution. This work represents the capstone experimental demonstration of the NASA University Leadership Initiative (ULI) project on SNLF technology.

Keywords: Slotted, natural-laminar-flow (SNLF) wing, NASA Ames 11-Foot Transonic Wind Tunnel (11-FT TWT), laminar-turbulent transition

1. Introduction

Skin-friction drag arising from turbulent boundary layers represents a dominant contribution to the total aerodynamic drag of commercial transport aircraft [1]. Maintaining laminar flow over the wing surface, and thus delaying or eliminating the laminar-to-turbulent transition, is one of the most impactful strategies available to reduce fuel burn and emissions without fundamental changes to the aircraft configuration. Among the passive approaches to maintaining laminar flow in absence of significant crossflow, the natural-laminar-flow (NLF) concept achieves transition delay by shaping the airfoil to promote a strong favorable pressure gradient over the majority of the chord, which suppresses the

Tollmien-Schlichting (TS) instability, the primary transition mechanism in the boundary layer [2, 3], by keeping the boundary-layer profile full and stable. However, the extent of the favorable pressure gradient that a conventional NLF airfoil can sustain is constrained by the requirement that the pressure must recover to a near-freestream value at the trailing edge, which limits how far the TS-stabilizing gradient can reach along the chord.

The slotted, natural-laminar-flow (SNLF) concept, embodied in the S207 airfoil designed by Somers [4], relaxes this constraint through a permanent slot near the trailing edge that divides the wing into fore- and aft-elements. By eliminating the requirement that the pressure on the upper surface of the fore element returns to the near-freestream value at its trailing edge, the slot extends the region over which a favorable pressure gradient can be sustained on both sides of the fore element. This extended favorable gradient suppresses TS amplification along a greater fraction of the chord than is achievable with a conventional NLF design.

Although a favorable pressure gradient stabilizes the TS instability, it destabilizes the crossflow (CF) instability if the wing is sufficiently swept, which is desirable for increasing the cruise Mach number. The aerodynamic viability of the SNLF concept was therefore established through a series of computational boundary-layer stability analyses conducted as part of a NASA University Leadership Initiative (ULI) project. Groot et al. [5] and Heston et al. [6] analyzed the amplification of TS disturbances on the S207 airfoil across the full design angle-of-attack range at flight conditions, and determined that a sweep angle of $\Lambda = 12.5^\circ$ keeps both the TS and CF amplification N-factors subcritical throughout. The additional influence of the frequency bands known to be excited within the NASA Ames 11-Foot Transonic Wind Tunnel (11-FT TWT) was assessed, and $\Lambda = 12.5^\circ$ was selected as the configuration for experimental validation.

Building on this computational groundwork, an experiment was conducted in the 11-Foot Transonic Wind Tunnel facility (11-FT TWT) at NASA Ames Research Center [7]. The facility achieves conditions representative of full-scale transonic cruise, with the test matrix designed to bracket the reference point of $Re_c = 13 \times 10^6$ and $M = 0.7$. The model is a semi-span, untapered, swept wing that supports the S207 SNLF airfoil at a constant sweep angle of $\Lambda = 12.5^\circ$. The location of the laminar-to-turbulent transition region is measured by means of infrared (IR) thermography, and the surface pressure distribution is captured through static pressure ports, on both the suction and pressure sides of the wing. Together, these measurements enable a direct comparison against boundary-layer stability computations.

This article aims to demonstrate that, at full-scale transonic conditions in the NASA Ames 11-FT TWT facility, the SNLF technology enables stabilizing the TS instability on the suction side of the fore element to such an extent that practically the entire suction side of the fore element supports laminar flow. Although measurement data are available for the pressure side, this article is focused on the suction side of the fore element. Two technical contributions are implemented toward this end. First, the methodology used to extract the transition-region location from the IR thermography data is carefully described: this includes the masking of unavoidable measurement artifacts and the gradient-based algorithm used to fit the transition region and quantify its temporal uncertainty from the time-resolved video frames. Second, the stability analysis pipeline that supports the interpretation of the measurements is presented: the measured C_p-distributions are fed into the boundary-layer code DEKAF [8, 9] to reconstruct the laminar base flow, and Linear Parabolized Stability Equations (LPSE) are solved with EPIC [10] to compute TS N-factor isocontours that are compared directly against the IR-measured transition locations, as per the traditional e^N-method [11, 12, 13, 14]. This work represents the capstone experimental demonstration of the NASA ULI project.

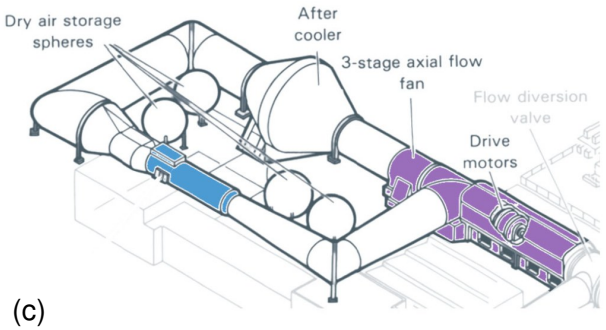
2. Facility & Model

The details of the facility, model and instrumentation are presented next. For a broader coverage of the wind-tunnel campaign, see Coder [7].

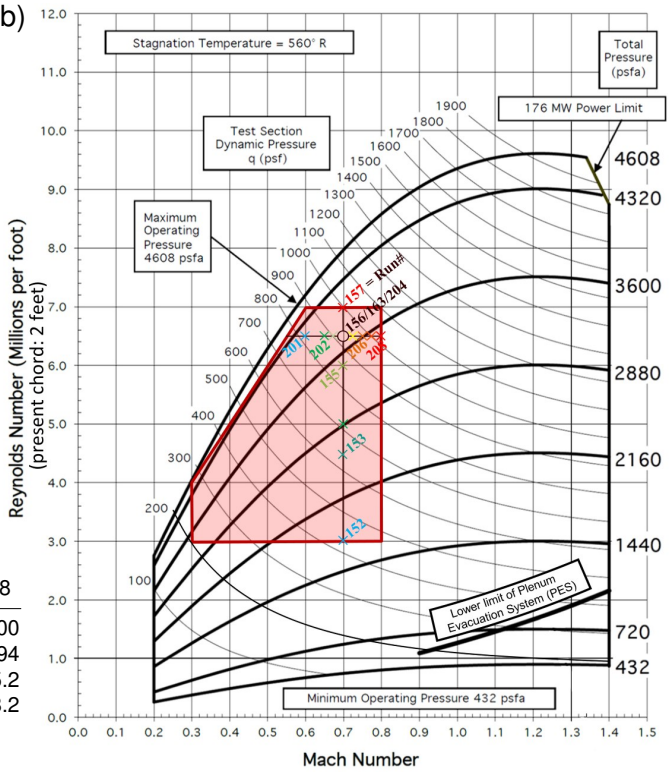
2.1 NASA Ames 11-FT Transonic Wind Tunnel

The experiment was conducted in the 11-Foot Transonic Wind Tunnel (11-FT TWT) facility at NASA Ames Research Center [15], in early 2022. The facility lay-out is shown in Fig. 1(a). The facility is a closed-circuit, variable-pressure wind tunnel capable of continuous operation across a transonic

(a)



(b)



(c)

Run #	156	152	153	155	157
M	0.700	0.700	0.700	0.700	0.700
$Re_c/10^6$	12.94	5.972	8.957	11.94	13.93
p_∞ (kPa [abs])	122.7	55.01	83.10	112.5	132.5
T_∞ (K)	272.3	266.4	267.8	270.9	293.1

Run #	163	201	202	204	206	208
M	0.700	0.600	0.650	0.700	0.750	0.800
$Re_c/10^6$	12.94	12.94	12.94	12.94	12.94	12.94
p_∞ (kPa [abs])	122.8	144.6	133.4	123.2	113.6	105.2
T_∞ (K)	272.5	274.5	274.5	273.2	270.7	268.2

Figure 1 – (a) Schematic of the facility containing the 11-FT TWT at NASA Ames [15], with the test section (blue) and drive motors (purple) highlighted. (b) Test matrix covering cruise conditions in the M–Re' plane; reference point: $(M, Re_c, Re') = (0.7, 13\times10^6, 6.5\times10^6/\text{ft})$, see Ref. [16] for more information on the chart. (c) Table of freestream parameters.

Mach number range of $0.2 \le M \le 1.4$ at sufficiently high unit Reynolds numbers to be representative of flight for a half-span model. The test section features slotted walls that connect to a surrounding plenum; these slots, together with the drive train, constitute the primary known sources of freestream disturbances. Flow-quality measurements reported by Amaya & Murthy [17] identify a contribution in the range of 2.5–3.0 kHz attributed to wall slots (shown in Fig. 2) and a drive-train contribution in the range of 180–650 Hz, depending on Mach number. The test matrix, focused on cruise conditions for which laminar flow is relevant, is shown in Fig. 1(b) and covers a range of chord Reynolds numbers and angles of attack bracketing the reference point of $Re_c = 13\times10^6$ and $M = 0.7$.

2.2 Model

The model consists of a two-element, semi-span, untapered, swept wing supporting the S207 SNLF airfoil [4] at a constant sweep angle of 12.5°, see Fig. 2. The leading-edge-orthogonal chord is 609.6 mm (2 ft) and the span is 1.676 m (5.5 ft). A fairing encloses the root of the model at the tunnel floor. The aft element is supported by three brackets; for the present study, the slot was open.

The model is instrumented with 210 static pressure taps distributed across three leading-edge-orthogonal rows in a 60/90/60 arrangement, on both the fore and aft elements and on both the suction and pressure sides. The pressure-tap rows on the fore element provide the surface pressure distributions used as input to the stability analysis. Infrared thermography is performed using four cameras, two viewing the suction side and two viewing the pressure side of the fore element, through Germanium windows mounted in the wind-tunnel wall slots also seen in Fig. 2.

To ensure adequate thermal contrast for the IR cameras, the model surface was coated with a high-emissivity, matte black paint by the vendor, while accounting for the paint-layer thickness in the milling process. As the paint itself left a relatively rough finish, the surface was sanded and a profilometer indicated its roughness was $0.45\,\mu\text{m}$, corresponding to a roughness Reynolds number $Re_{kk} \approx 1$. This ensures that roughness-induced transition contamination remains negligible [18, 19].

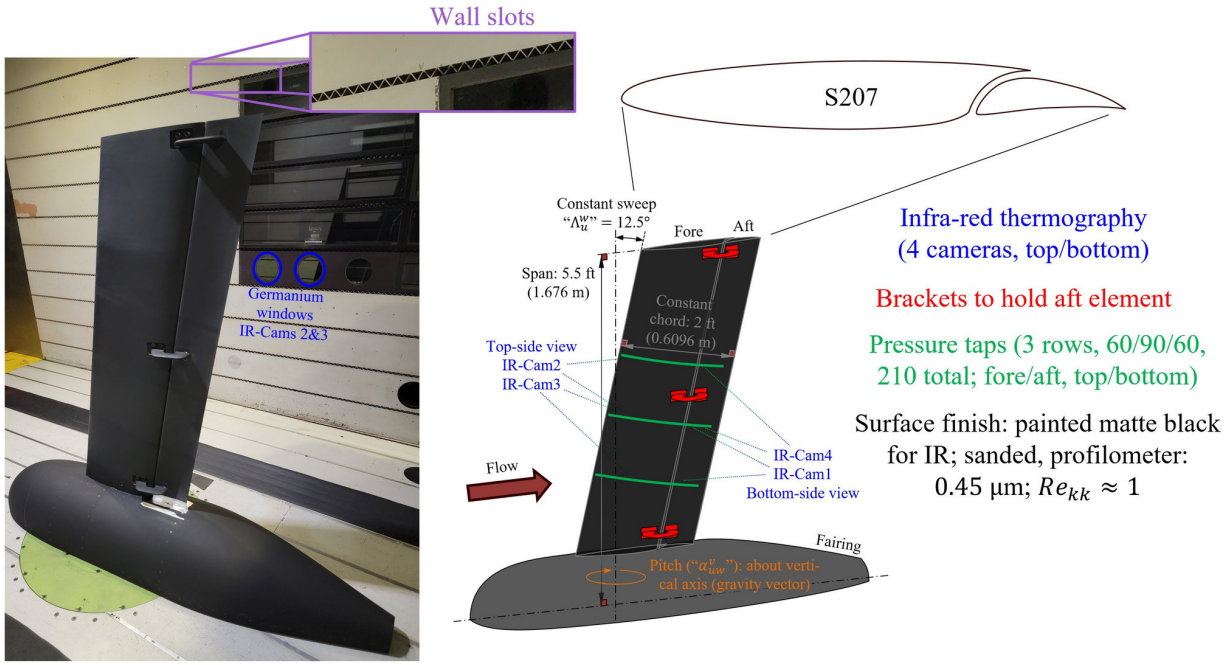


Figure 2 – The S207 semi-span, untapered, swept-wing model installed in the NASA Ames 11-FT TWT facility (left) and a schematic of its geometry and instrumentation (right). The Germanium windows through which IR-Cams 2 and 3 view the suction side of the fore element are visible in the tunnel wall. The brackets holding the aft element in the open-slot configuration and the three leading-edge-orthogonal pressure-tap rows are indicated in red and green, respectively.

3. Post-Processing

The location of the transition region and boundary-layer stability were determined as follows.

3.1 Transition Region

The location of the transition region was extracted from the IR thermography videos on a frame-by-frame basis. The processing pipeline consists of four elements: mean-frame subtraction, artifact masking, transition-line detection via a Hough transform, and angle-of-attack extraction.

3.1.1 Mean-Frame Subtraction

To enhance the thermal contrast associated with the transition region and suppress stationary background features, a temporal mean frame is computed by averaging the raw pixel intensities over a carefully selected range of frames corresponding to conditions at which the transition region is known to be absent. This mean frame was then subtracted from each individual frame prior to further analysis. The subtraction effectively removes the steady thermal background, including gradients due to non-uniform illumination, model surface emissivity variations, and camera artifacts. In doing so, the spatially sharp thermal signature of the transition front stands out as the dominant feature, if the remaining artifacts are furthermore masked.

3.1.2 Artifact Masking

Following mean-frame subtraction, unavoidable artifacts that could corrupt the transition-region detection were masked, as shown in Fig. 3. The artifacts addressed include:

- turbulent wedges (green lines in Fig. 3) produced by the leading-edge-orthogonal pressure-port rows (blue lines), which arise because the surface in the immediate vicinity of the port holes was not sanded and thus carries a locally elevated roughness;
- the region upstream of and including the leading edge of the fore element (red line), whose appearance is affected by the averting surface curvature;

- the region downstream of and including the unpainted trailing-edge strip of the fore element (red line), whose surface finish and geometry produce a thermal signature unrelated to transition;
- the reflection of the IR cameras in the model surface (yellow ellipses); and
- transient turbulent wedges that appeared and dissolved as small particles impacted the leading edge during a run (cyan lines).

Each transient wedge was individually masked for a given frame range: active only during the frames in which the contamination was observed. *Whenever the flow on the suction side of the fore element is claimed to be 'fully laminar', those regions of the flow that are not subject to the aforementioned artifacts are meant, i.e. the turbulent wedges generated by the pressure-port rows and particles that impacted the leading edge are ignored.*

By manually sanding the region around the pressure-port rows later in the campaign, the surface roughness was confirmed to be the culprit producing turbulent wedges, because they disappeared under certain conditions, e.g. low unit Reynolds numbers.

3.1.3 Transition-Line Detection

After masking, the transition region was identified using a column-based Hough transform [20, 21]. The mean-frame-subtracted and masked pixel-brightness field was first smoothed with a moving average of width 4 pixels in the chordwise (horizontal) direction and the chordwise gradient was computed using a fourth-order central finite-difference stencil:

$$\left.\frac{\partial I}{\partial X}\right|_j \approx \frac{-I_{j-2}+8I_{j-1}-8I_{j+1}+I_{j+2}}{12\Delta X}, \tag{1}$$

where I_j denotes the pixel brightness at column j and ΔX is the pixel spacing (in the direction parallel to the wind-tunnel walls). The transition region corresponds to the maximum absolute value of this gradient, since the laminar-to-turbulent transition produces the sharpest x-variation in surface temperature [22, 23]. A second pass of the same smoothing was applied to the gradient field prior to the Hough analysis.

The Hough transform operates as follows. For each candidate line angle θ in the range scanned, a column intercept coordinate X_i is assigned to the (X,Z)-coordinates of every above-threshold pixel, according to:

$$X_i = X - Z\tan\theta, \tag{2}$$

where X and Z are parallel and perpendicular to the tunnel floor, respectively, see Fig. 3 for a defining illustration. A histogram of X_i-values is accumulated over all such pixels. A strong, spatially coherent transition front at angle θ produces a sharp peak in this histogram at the corresponding intercept value X_i. The two-dimensional accumulator array $\mathcal{N}(\theta,X_i)$ is smoothed independently in both the angle and intercept directions before peak detection. Only grid points that are a local maximum in both θ and X_i simultaneously qualify as valid detections. Spurious nearby peaks are suppressed by zeroing out an elliptical neighborhood around each accepted peak.

The dominant peak in $\mathcal{N}(\theta,X_i)$ yields the best-fit angle θ^* and intercept X_i^* of the transition line for the current frame. The width of the peak in the intercept direction, defined as the range of X_i over which $\mathcal{N}$ remains within 10% of its maximum value for fixed $\theta=\theta^*$, is adopted as a measure of the width of the transition region. The two bounding lines $X_i = X_i^* \pm \delta X_i$ are taken as the upstream and downstream edges of the transition region; they are shown as the magenta lines in Fig. 3. These bounds correspond approximately to the spanwise-averaged intermittency region between the onset of transition and breakdown. The extent of this region is estimated from the width of the Hough peak, across which the thermal gradient associated with transition is detectable.

For comparison with the stability results, the transition locations are needed at the pressure-port locations. Therefore, the chordwise positions at which the transition region intersects the inner edge of each pressure-port row are then determined geometrically by computing the intersection of the fitted transition positions with the known pixel-coordinate representation of each port row, and are converted to leading-edge-orthogonal chord fractions x/c using the pixel locations of the leading and

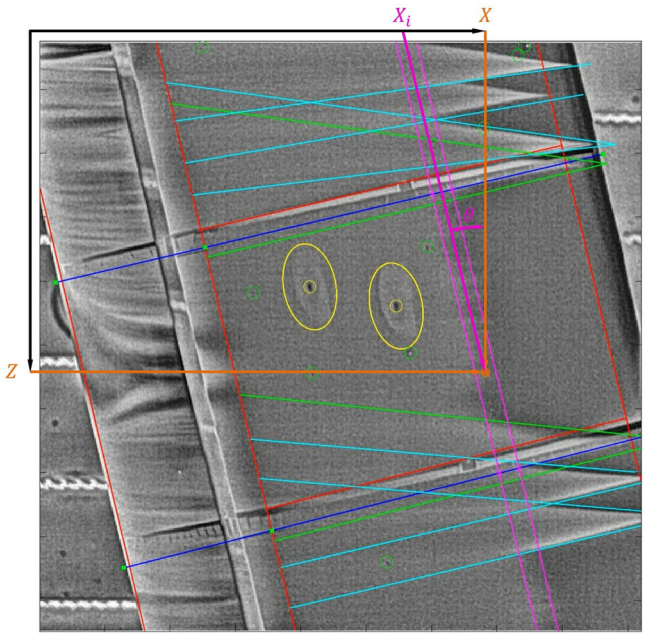


Figure 3 – Infra-red thermography frame displaying transition region (magenta *lines*, approximating the upstream and downstream extents of the spanwise-averaged intermittency region between the onset of transition and breakdown) captured in-between the Mid- (on bottom) and Outboard (top) pressure-tap rows (blue lines) with unavoidable artifacts masked (green, cyan, red, and yellow lines) for Run #204 at AoA $= 1.384°$. Pixel coordinates X, Z (black and orange arrows), intercept coordinate X_i and scanning angle θ (magenta *arrows*) as related through Eq. (2). Flow is from right to left.

trailing edges of the fore element. A sweep-angle correction is applied to account for the apparent perspective difference between the true model sweep angle and the sweep angles of the leading edge and pressure-port rows as seen by each camera.

No image unwarping was performed. Since the present analysis only requires the chordwise coordinate x/c, determined from the projected leading- and trailing-edge locations, the transition position can be obtained directly from the projected chordwise coordinate after application of the sweep-angle correction. Any remaining discrepancy between projected and surface coordinates is considered negligible compared to the uncertainty in the transition-location determination.

3.1.4 Angle-of-Attack Extraction

Each video frame displays the angle of attack as rendered by the wind-tunnel data acquisition system. To associate every frame with its corresponding angle of attack as accurately as possible and link it to the IR-measurement data, this value was extracted automatically using optical character recognition (OCR). Since a small delay exists between the displayed angle-of-attack value and the IR video feed, a frame-offset correction is applied to synchronize the two signals. The angle of attack was set statically: the model was pitched to each angle of attack and held fixed for a period of time, while IR video frames were acquired continuously. The mean transition-region location and its standard deviation reported in the results therefore reflect the temporal variability of the transition region at a fixed angle of attack, rather than any dynamic pitching effect. This is key to select appropriate frames with which to accurately establish the transition region and its standard deviation across the sampling time for a given angle of attack.

3.2 Boundary-Layer Stability Analysis

To analyze the instability mechanisms of the boundary layer, the C_p-distributions are used as input to the boundary-layer solver DEKAF, whose results are then used to compute amplification factors with the Linear Parabolized Stability Equation (LPSE) solver EPIC.

3.2.1 Pressure Distributions

Because the swept-wing boundary-layer development is governed primarily by the leading-edge-orthogonal velocity component, the pressure distributions are presented using the transformed coefficient:

$$C_p = \frac{p - p_\infty}{\frac{\gamma}{2} p_\infty M^2 \cos^2 \Lambda_{uv}^w}, \quad \text{where:} \quad \Lambda_{uv}^w = \arcsin\left(\sin \Lambda_u^w \cos \alpha_{uw}^v\right), \tag{3}$$

with $\Lambda_u^w = 12.5^\circ$ and AoA $= \alpha_{uw}^v$ the angles illustrated in Fig. 2; the latter is recorded as the angle of attack in the experiment. This C_p-definition is chosen because it preserves the pressure gradient experienced by the boundary layer in the leading-edge-orthogonal direction. While the measured aerodynamic coefficient based on total freestream dynamic pressure is $C_p \cos^2 \Lambda_{uv}^w$, the transformed coefficient is the direct input for the boundary-layer calculation and the correct version to facilitate interpreting trends in the stability analysis results. To allow recomputing Λ_{uv}^w in Eq. (3), α_{uw}^v will be reported up to the precision available from the measurement data. Following this definition, the attachment-line (0) and sonic ($*$) values are:

$$C_{p,0} = \frac{2}{\gamma M^2 \cos^2 \Lambda_{uv}^w} \left[\left(1 + \frac{\gamma - 1}{2} M^2 \cos^2 \Lambda_{uv}^w \right)^{\frac{\gamma}{\gamma - 1}} - 1 \right] \geq 1, \tag{4}$$

$$C_p^* = \frac{2}{\gamma M^2 \cos^2 \Lambda_{uv}^w} \left[\left(\frac{2 + (\gamma - 1) M^2 \cos^2 \Lambda_{uv}^w}{\gamma + 1} \right)^{\frac{\gamma}{\gamma - 1}} - 1 \right]. \tag{5}$$

3.2.2 Boundary-layer flow: DEKAF

By feeding the measured C_p-distributions into the compressible boundary-layer solver DEKAF [5, 8, 9], an accurate laminar base flow is reconstructed from the experimental data. For each spanwise pressure-port row and angle of attack, the discrete tap measurements are interpolated onto a fine arc-length grid using spline interpolation and subsequently mapped onto a 2000-node leading-edge-orthogonal marching grid with hyperbolic-tangent clustering toward the attachment line. The attachment-line location is identified as the C_p-maximum, and a minor isentropic correction is applied in its vicinity to ensure that the splined distribution does not overshoot its theoretical stagnation value. The non-self-similar compressible boundary-layer equations are then marched downstream, assuming an adiabatic wall, a calorically perfect gas, and Sutherland's law for viscosity, with freestream thermodynamic properties derived from the tunnel operating conditions. Although this is expected to be moderately stabilizing only for the TS instability [24, Fig. 3.13], the leading-edge-orthogonal curvature of the fore element surface, computed from the airfoil geometry, is extracted using a similar procedure and is accounted for in the stability analysis.

3.2.3 Linear Parabolized Stability Equations (LPSE): EPIC

The stability of the boundary layer is analyzed for three-dimensional Tollmien-Schlichting waves using the Linear Parabolized Stability Equations (LPSE) as implemented in EPIC [10], with the base-flow velocities oriented in a leading-edge-orthogonal coordinate system. Disturbance variables q' take the form of traveling waves with complex chordwise wavenumber α (in the leading-edge-orthogonal direction), real spanwise wavenumber β (in the leading-edge-parallel direction), and real angular frequency ω in radians per second (the cyclic frequency in Hertz: $f = \omega/2\pi$) described by the ansatz:

$$q'(x,y,z,t) = \hat{q}(x,y) \mathrm{e}^{\mathrm{i}\left(\int^x \alpha(\bar{x})\mathrm{d}\bar{x} + \beta z - \omega t\right)} + c.c., \tag{6}$$

where $\bar{x}$ is the integration-variable equivalent of x and $c.c.$ denotes the complex conjugate. The shape functions $\hat{q}$ vary slowly in the leading-edge-orthogonal x-direction, which allows neglecting their second x-derivatives, thereby parabolizing the equations. Spatial disturbance amplification in the downstream direction is of main interest, which is recovered in $-\alpha_i(x)$ upon imposing a real (ω, β)-combination. Disturbance amplification is then quantified with N-factors:

$$N(x) = -\int_{x_n}^{x} \alpha_i(\bar{x})\, \mathrm{d}\bar{x} + \frac{1}{2} \ln \frac{\tilde{E}(x)}{\tilde{E}(x_n)}, \tag{7}$$

where $-\alpha_i$ is the growth rate in the leading-edge-orthogonal direction, x_n is the neutral point where $\mathrm{d}N/\mathrm{d}x = 0$, and $\tilde{E}(x)$ is the Chu norm of the disturbance shape functions [25]:

$$\tilde{E}(x) = \int \left(\overline{\rho}(x,y) \left(|\hat{u}(x,y)|^2 + |\hat{v}|^2 + |\hat{w}|^2 \right) + \frac{\overline{\rho}}{\gamma(\gamma-1)M^2\overline{T}} |\hat{T}|^2 + \frac{\overline{T}}{\gamma M^2 \overline{\rho}} |\hat{\rho}|^2 \right) \mathrm{d}y, \tag{8}$$

where overbars denote local base-flow quantities, $\overline{\rho}$, $\overline{T}$ are the base-flow density and temperature, γ is the ratio of specific heats, and M is the freestream Mach number. The hatted quantities $\hat{u}$, $\hat{v}$, $\hat{w}$, $\hat{T}$, and $\hat{\rho}$ are the complex disturbance shape functions of the leading-edge-orthogonal, wall-normal, and spanwise velocity components, temperature, and density, respectively. The auxiliary condition, that is used to minimize the x-variation of the shape functions consistent with the parabolizing approximation, is also based on the Chu norm. For this study, the LPSE approach was not stabilized: the $\partial\hat{p}/\partial x$-term was kept and the convergence of all (ω,β)-combinations defining the N-factor envelope in terms of both the auxiliary condition and the resolution in the x-direction was ensured.

The N-factor envelope at each chordwise location is formed by maximizing N over all computed (ω,β)-combinations, representing the most amplified disturbance at that station. The envelopes attributed to the 'streamwise' Tollmien-Schlichting (TS-)instability mechanism were carefully captured, which was done by sweeping over the frequencies and spanwise wavelengths reported in Tab. 1. Solutions with a low frequency, f, and large spanwise wavelength, λ_z, are subject to the stepsize criterion inherent to the LPSE approach. While the resolution in the x-direction was set such that these solutions never determined the N-factor envelope (as calculated when stabilized by dropping the $\partial\hat{p}/\partial x$-term), they were removed to avoid artifacts in the N-factor envelopes (when stabilization was deactivated: keeping the $\partial\hat{p}/\partial x$-term). As discussed in more detail by Heston et al. [6] for the computational-companion study in similar conditions, the content representative of the TS-instability usually has waveangles that are not more than 65° removed from the inviscid streamline direction. Due to the low sweep ($\Lambda_u^w = 12.5^\circ$), N-factors associated to the stationary ($\omega = 0$) crossflow instability were found to be negligible ($N < 0.5$, tested for Run #156, AoA $= 2.989^\circ$).

4. Results

The results are organized as follows. The reference condition ($M = 0.7$, $Re_c = 13\times10^6$) is addressed first, covering two repeated runs to establish repeatability and to demonstrate the agreement between the IR-measured transition locations and the LPSE N-factor isocontours across all three spanwise pressure-port rows (In-, Mid-, and Outboard). After evaluating the laminar flow on the SNLF wing for a range of angles of attack at the reference condition ($M = 0.7$, $Re_c = 13\times10^6$), it is demonstrated next that this is not an exceptional result, by independently varying the Reynolds and Mach number.

4.1 Overview for the Reference Condition

The reference condition corresponds to $M = 0.7$ and $Re_c = 13\times10^6$. The C_p-distributions for this case are given in Fig. 4. In Fig. 4(a), the variation with the angle of attack is given. Most notable is the favorable pressure gradient sustained over the majority of the fore element for AoA $\leq 1^\circ$, with the suction-side C_p remaining nearly constant at approximately $x/c = 60\%$ before the pressure recovery begins. This extended favorable gradient is the key feature that suppresses TS amplification over the fore element. For AoA $\geq 2.5^\circ$, the critical Mach number is exceeded and a supersonic pocket develops on the leading edge. For AoA $\geq 4^\circ$, a supersonic plateau develops near the leading edge and terminates abruptly, marking the foot of a shock wave, which takes the flow back to subsonic conditions.

The repeatability of the C_p-distributions is demonstrated with Runs #156 and #163 and a general representation of the spanwise variation across the In-, Mid-, and Outboard pressure-port rows is

Table 1 – (Cyclic) frequencies (f) and spanwise wavelengths (λ_z, all positive) used to form the N-factor envelope; the number above the arrows denotes the spacing in the same unit.

$f = \frac{\omega}{2\pi}$ (kHz):	$2 \xrightarrow{0.5} 3$	$4 \xrightarrow{1} 12$	$14 \xrightarrow{2} 36$
$\lambda_z = \frac{2\pi}{\beta}$ (mm):	$2 \xrightarrow{1} 6$	$8 \xrightarrow{1.5} 12.5$	

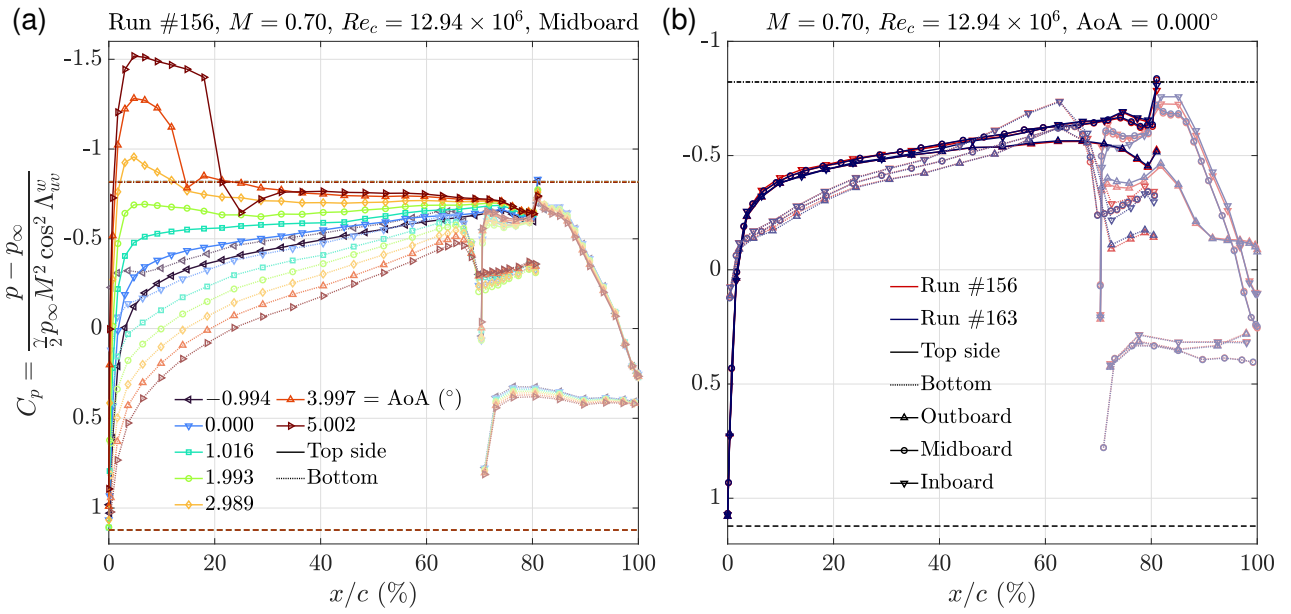


Figure 4 – Leading-edge-orthogonal C_p-distributions (a) for a variety of angles of attack (AoA $= \alpha_{uw}^v$) along the Midboard pressure-port row for Run #156; (b) for all pressure-port rows (In-, Mid-, and Outboard) for Runs #156 and #163 at AoA $= 0°$. Distributions corresponding to the bottom of the fore element and those for the aft element (desaturated colors). Attachment-line (horizontal dashed line) and sonic (horizontal dash-dotted line) C_p-values.

shown in Fig. 4(b). On the suction side, the measured C_p-distributions along the In- and Midboard rows are practically the same, while the Outboard row recovers sooner, with pressure recovery beginning around $x/c \approx 50$–55% compared to $x/c \approx 65$–70% for the other two rows. The three spanwise rows are in close agreement for $x/c < 40\%$, which strongly supports the infinite-wing assumption underpinning the DEKAF and EPIC analyses. The Mid- and Outboard distributions are very closely recovered from Run #156 to #163, with the difference undetectable for $x/c < 50\%$. A slightly stronger expansion occurs along the Inboard row for Run #156 relative to #163, with $\max \Delta C_p = 0.0297$. Although only AoA $= 0°$ in Fig. 4(b) is shown, a very similar ΔC_p is observed at other angles of attack.

Honoring Van Ingen [12, Fig. 9.19] and [11, Fig. 9], the measured location of the transition region (symbols connected by solid lines and patches) and stability results (colored N-isocontours) for Runs #156 and #163 in Figs. 5 and 6, respectively, is presented here similarly. Whereas the symboled lines indicate the mean transition-region location in time, the patches indicate its uncertainty in time (plus/minus two standard deviations), i.e. across the number of frames in the IR-thermography video corresponding to a given angle of attack. These figures furthermore show the shock-wave location (symbols connected with dashed lines) and the location corresponding to incipient separation as detected by the boundary-layer solver (black dashed line). For these Runs, data were processed for all three pressure-port rows and for a pitch-spacing of ΔAoA $= 0.125°$.

The shock-wave locations shown in Figs. 5 and 6 are identified by visual inspection of the IR thermography frames and should be regarded as indicative rather than definitive. The N-factor isocontours are not plotted downstream of the shock location, since the boundary-layer and stability assumptions break down there. The incipient separation locations detected by DEKAF are retained in the figures, but should be interpreted with caution: the spacing between the pressure taps is likely too large to accurately represent the adverse pressure gradient associated with the shock. That gradient is almost certainly underestimated, allowing DEKAF to continue marching past the shock without detecting separation.

Considering Figs. 5 and 6, the transition region moves upstream with increasing angle of attack, in accordance with the C_p-distribution becoming progressively less favorable: the favorable gradient is sustained over a shorter chordwise extent and the pressure recovery begins earlier, providing less stabilization of the TS instability. As the angle of attack is decreased toward $0°$, the transition region moves downstream until it passes the location where DEKAF detects incipient laminar separation in

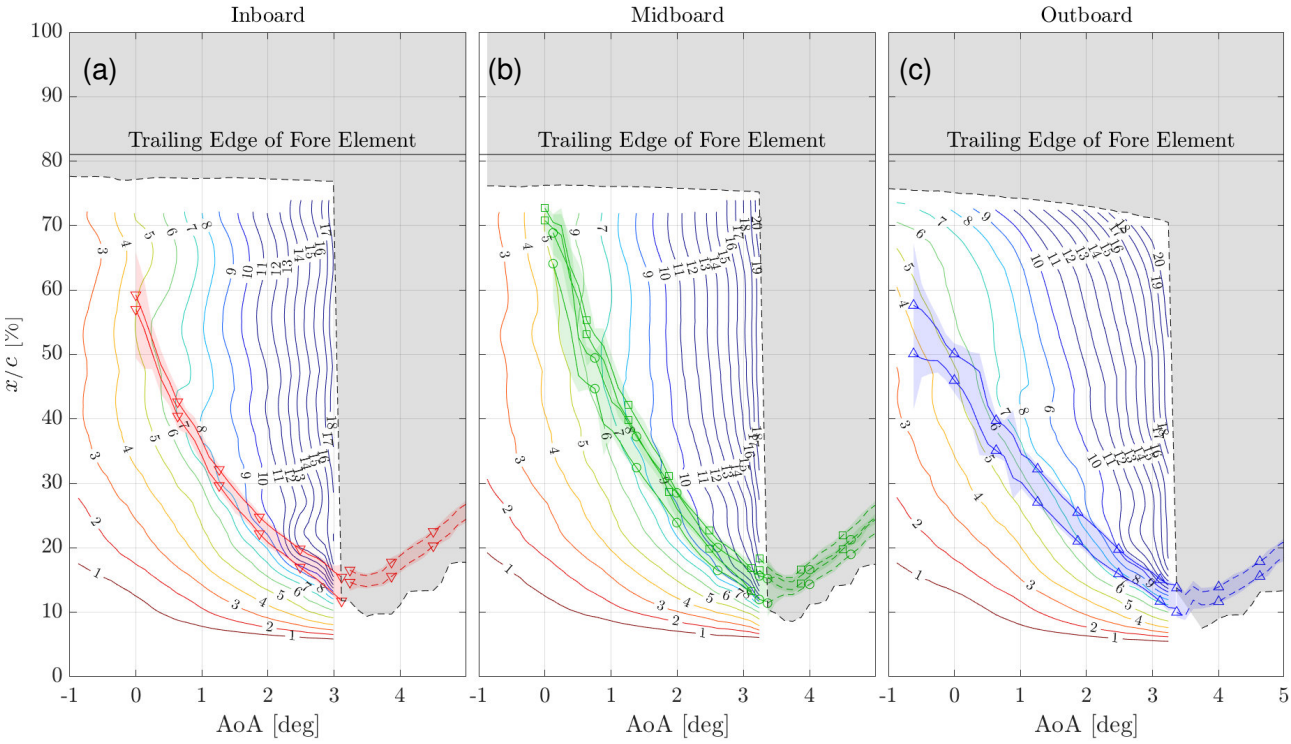


Figure 5 – Comparison of the location of transition region (symbols connected by solid lines; patch: uncertainty in time, $\pm 2\sigma$) against LPSE N-factor isocontours (colored lines) for the In- (a), Mid- (b, circle: Outboard camera Cam2; square: Inboard camera Cam3), and Outboard (c) pressure-port rows on the top (suction) side corresponding to Run #156: $M = 0.7$, $Re_c = 13 \times 10^6$ (ΔAoA $= 0.125°$). Locations of shock wave (symbols connected by dashed lines) and incipient separation as detected by DEKAF (dashed black line).

the pressure recovery region near the trailing edge of the fore element. At that point, the favorable gradient ends and the boundary layer, still laminar at that stage, encounters an adverse gradient it cannot sustain. This marks the practical limit of the fully laminar fore element. Practically fully laminar flow over the suction side of the fore element is thus achieved for angles of attack ranging from $-1°$ to $0°$. IR-images corresponding to angles of attack that support fully laminar (panels (a) & (c)) versus transitional (b,d) flow for both Runs #156 (a,b) and #163 (c,d) are given in Fig. 7. The transition front for the Outboard pressure-port row for Run #163 is terminated relatively far upstream ($x/c \approx 40\%$) for angles of attack up to AoA $= 0.375°$, because a transient turbulent wedge obscured its continued downstream progression as illustrated in Fig. 8.

For Runs #156 and #163, the N-factor at which the transition region occurs ranges from $N = 4$–5 at low angles of attack, where the transition region lies near the trailing edge of the fore element, up to $N = 9$–10 at higher angles of attack, where the transition region lies further upstream. The N-factor at which the transition region occurs thus increases as the transition front moves upstream, a trend that is not immediately obvious and that, as can be observed to a lesser extent in the original results of Van Ingen [12, Fig. 9.19] and [11, Fig. 9], deserves a deeper investigation beyond the scope of the present article. For the purposes of transition prediction, a conservative lower bound of $N = 4$–5 is appropriate: the transition region typically lies downstream of the $N = 5$ isocontour. An important related feature is that the N-factor isocontours become nearly vertical in the rooftop region of the fore element, i.e. approximately constant in x/c across a range of angles of attack. This behavior is consistent with the C_p-distribution going through an inflection point in the rooftop region, defined here as the region of nearly constant C_p on the suction side of the fore element, visible for AoA $\lesssim 1°$ in Fig. 4(a). Downstream of $x/c \approx 40\%$, the pressure distribution becomes increasingly more favorable, further reducing the local TS growth rates and causing the N-factor envelope to plateau in the chordwise direction. A practical consequence is that the transition location based on a fixed critical N-factor is highly sensitive to small changes in the angle of attack where the critical

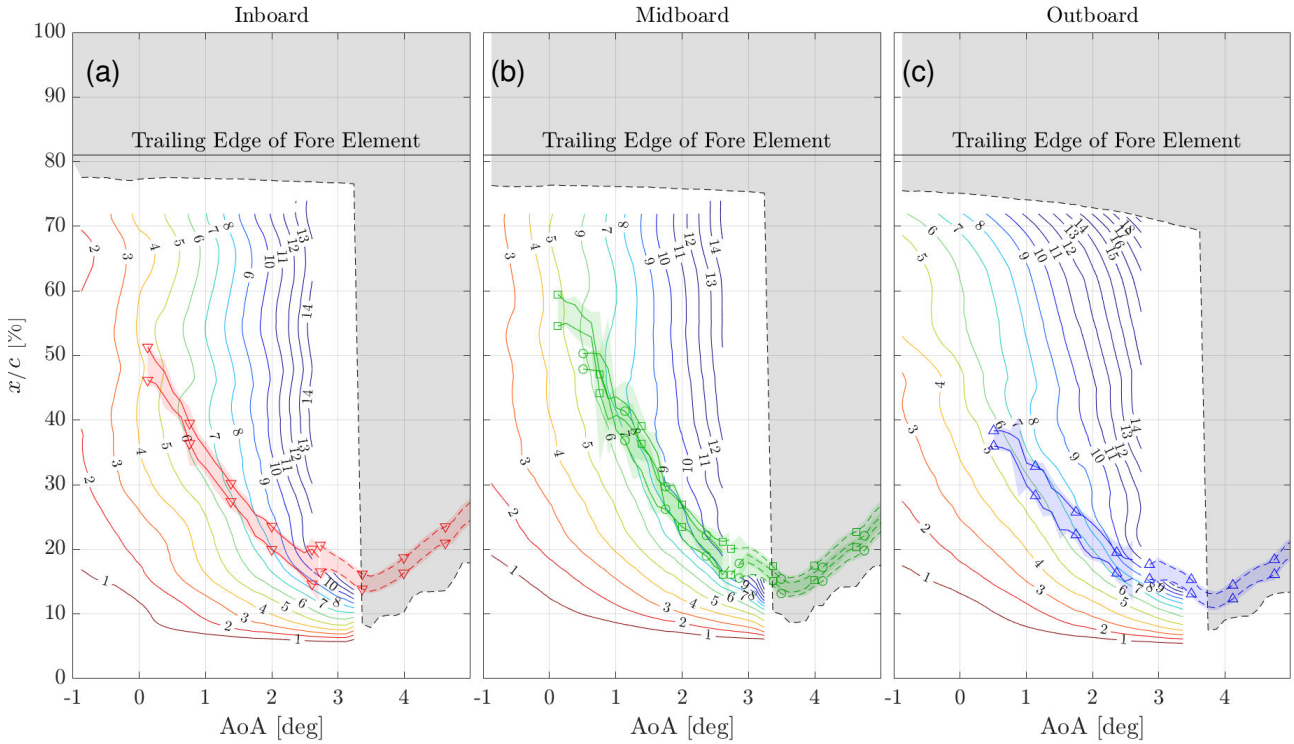


Figure 6 – Comparison of the location of transition region (symbols connected by solid lines; patch: uncertainty in time, $\pm 2\sigma$) against LPSE N-factor isocontours (colored lines) for the In- (a), Mid- (b, circle: Outboard camera Cam2; square: Inboard camera Cam3), and Out (c) pressure-port rows on the top (suction) side corresponding to Run #163: $M = 0.7$, $Re_c = 13 \times 10^6$ (ΔAoA $= 0.125°$). Locations of shock wave (symbols connected by dashed lines) and incipient separation as detected by DEKAF (dashed black line).

N-factor is reached in the rooftop region, since a small AoA perturbation causes a large chordwise shift in the transition front when the isocontours are nearly vertical. This sensitivity is an undesirable characteristic of the current airfoil design that warrants attention in future design efforts.

The C_p-differences covered in Fig. 4(b) are reflected in the stability results. First, the earlier pressure recovery along the Outboard row ($x/c > 40\%$ for the shown AoA in Fig. 4(b)) versus the In- and Midboard rows ($x/c > 70\%$) results in continued growth for the former row (N-isocontours slant to the left in the x/c–AoA plane), while the N-factors remain approximately constant for $x/c > 40\%$ for the latter rows (N-isocontours become vertical). Second, the slightly stronger expansion for $x/c < 40\%$ along the Inboard row for Run #156 relative to #163 results in a downstream shift of the transition region in Run #156 of $\Delta x/c \approx 6\%$, upon comparing Figs. 5(a) and 6(a).

Having evaluated the laminar flow on the SNLF wing for a range of angles of attack at the reference condition ($M = 0.7$, $Re_c = 13 \times 10^6$), it is demonstrated next that this is not an exceptional result by independently varying the Reynolds and Mach number.

4.2 Variation with Reynolds number

The C_p-distributions for the range of Reynolds numbers are given in Fig. 9(a). As Re_c is decreased, the top-side C_p becomes more negative, reflecting a stronger favorable pressure gradient over the fore element. This trend is consistent across all angles of attack considered and is consistent with the general notion that a thicker boundary-layer displacement thickness at lower Reynolds numbers makes the body appear thicker to the inviscid flow [26], requiring the flow to accelerate more strongly around it. Although this C_p-variation is subtle, with the overall shape and chordwise extent of the favorable gradient remaining essentially unchanged across the Reynolds number range considered, the resulting stronger favorable pressure gradient has a stabilizing effect. Therefore, the transition front is expected to display a downstream movement with decreasing Reynolds number.

The variation of the transition-region location and N-factor isocontours with Reynolds number is

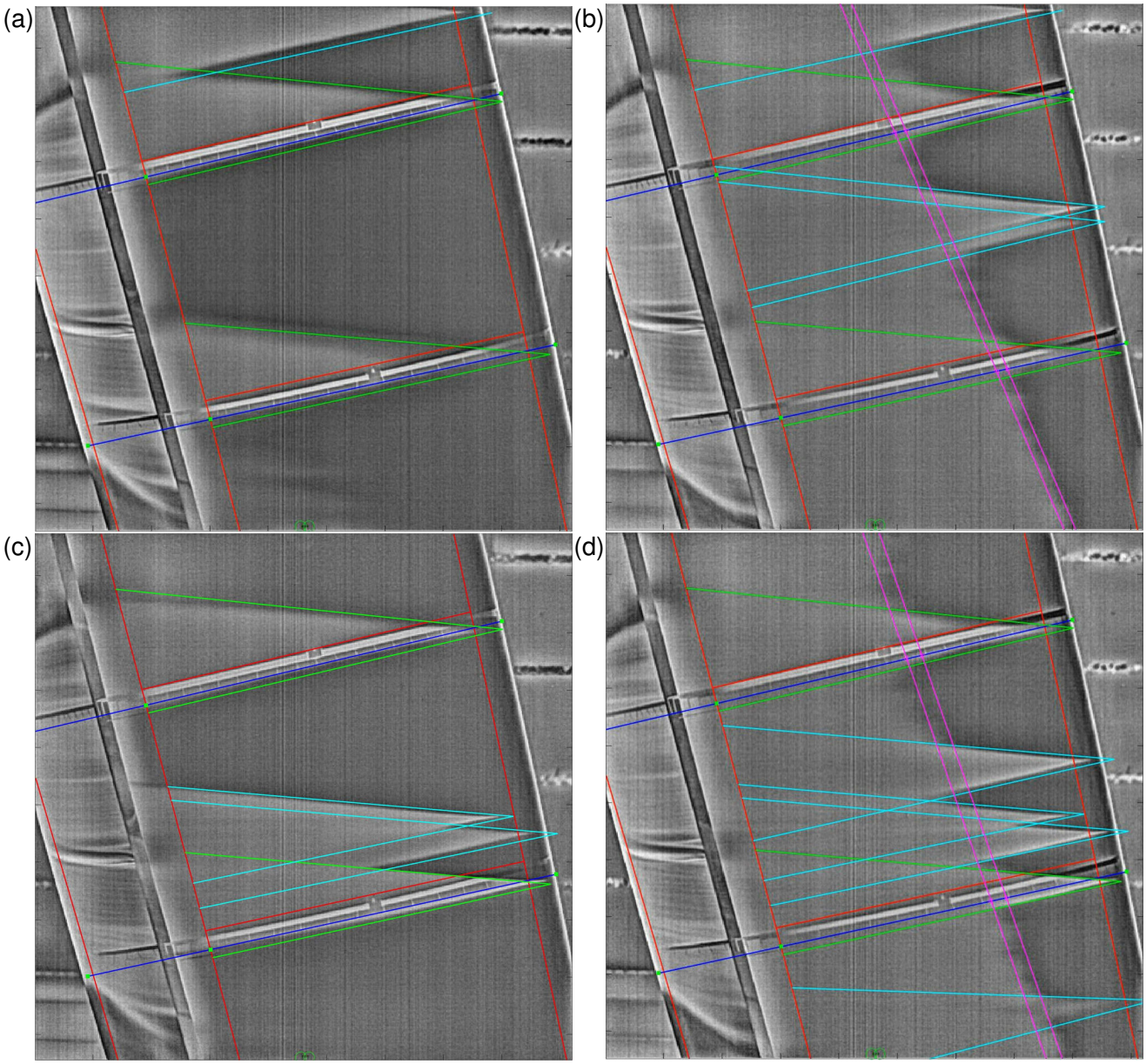


Figure 7 – Infra-red thermography frame displaying transition region (magenta lines) and masked artifacts for the In- (on bottom of each panel) and Midboard (top) pressure-tap rows during Run #156 (a,b) at AoA $= -0.374^\circ$ (a, fore element fully laminar) and 1.504° (b) and Run #163 (c,d) at AoA $= -0.374^\circ$ (c, fore element fully laminar) and 1.384° (d). Flow from right to left.

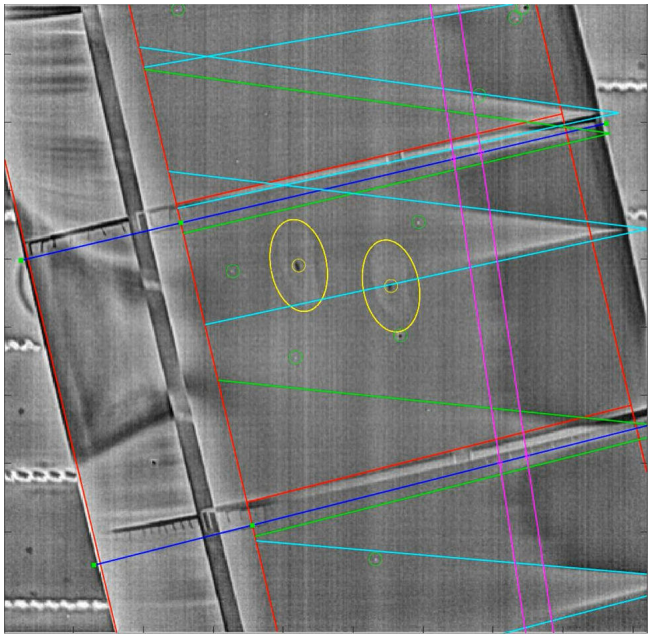


Figure 8 – Infra-red thermography frame displaying transition region (magenta lines) and masked artifacts for the Mid- (on bottom) and Outboard (top) pressure-tap rows during Run #163 at AoA $= 1.746^\circ$. Flow is from right to left. A transient turbulent wedge obscures the transition region (cyan lines) near the Outboard pressure-port row (top): as transition moves aft, it cannot be evaluated properly past $x/c = 40\%$ for that row.

given in Fig. 10. As the Reynolds number is decreased from 13×10^6 to 6.0×10^6, the upper bound of the angle of attack yielding fully laminar fore element at the Midboard row expands from AoA $= 0^\circ$ to 1°. The conservative critical N-factor of 4–5 consistently bounds the transition region from below across all Reynolds numbers considered.

4.3 Variation with Mach number

The TS instability is furthermore known to be stabilized with an increasing Mach number [2, 27], if all other factors are kept the same. While the variation of the C_p-distributions with the Mach number is shown in Fig. 9, the variation with the angle of attack for $M = 0.6$ and 0.8 is given in Fig. 11. The top-side C_p-distributions in Figs. 9(b) and 11 reveal that the pressure distribution varies significantly with Mach number.

At $M = 0.6$, the sonic C_p^*-value is more negative than for the reference condition and is crossed only at the highest angle of attack considered (AoA $= 5^\circ$), where a brief supersonic region develops near the leading edge. Across the angles of attack relevant to the laminar flow results, the flow remains entirely subsonic. The favorable gradient is noticeably weaker and shorter in extent than at the reference condition, with the suction-side C_p beginning to recover already around $x/c = 10$–15% for moderate angles of attack rather than sustaining the favorable gradient to $x/c \approx 60$–70%. At $M = 0.8$, by contrast, the fore element suction side is supersonic across the majority of its chord already at AoA $= -1^\circ$, and the favorable gradient is strong and chordwise-extended across all angles of attack considered. A shock appears as a sharp pressure discontinuity that moves progressively upstream from $x/c \approx 80\%$ at AoA $= 4^\circ$ to $x/c \approx 72\%$ at AoA $= 5^\circ$. As an aside, the fore element's bottom-side C_p-distributions also shift significantly with Mach number, crossing the sonic line at $M = 0.8$ for all considered angles of attack. As the Mach number increases, the top-side C_p-distributions generally become more favorable, hence TS is stabilized by both the inherent compressibility stabilization of the TS mechanism and the more favorable pressure gradient.

The variation of the transition-region location and N-factor isocontours with Mach number is given in Fig. 12. As the Mach number is increased from 0.6 to 0.75, the upper bound of the angle of attack yielding a fully laminar fore element expands from AoA $= -1^\circ$ to 1.5°. As the Mach number is pushed to 0.8, the flow is so stable that the full chord of the fore element is laminar up to AoA $=$

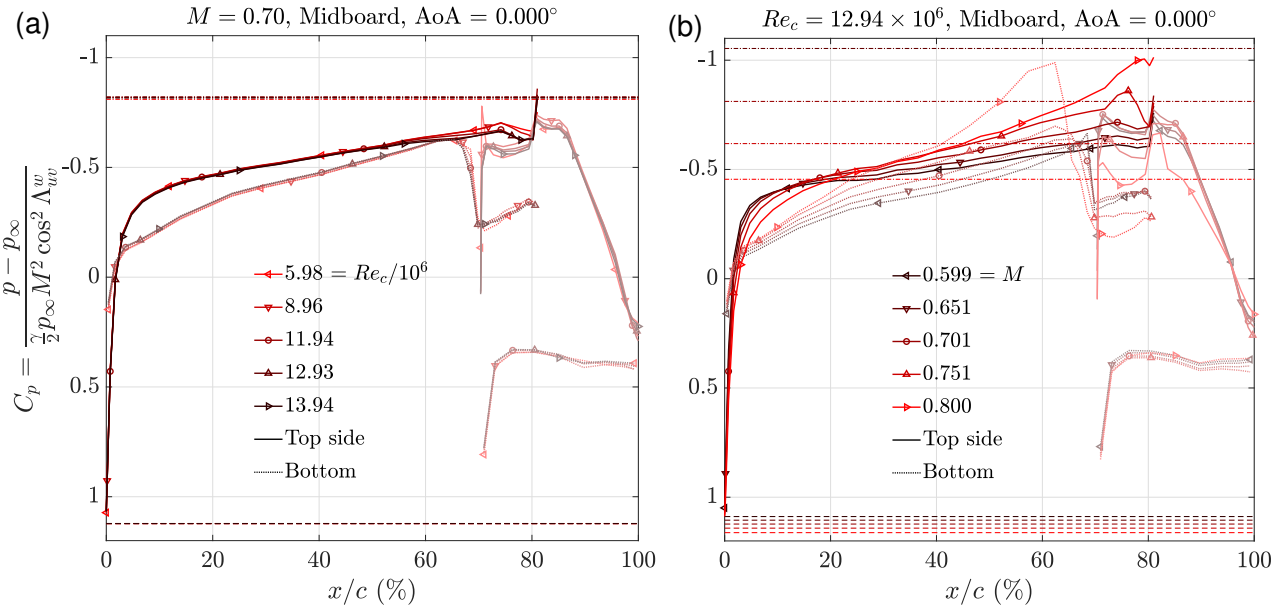


Figure 9 – Leading-edge-orthogonal C_p-distributions for a variety of (a) Reynolds and (b) Mach numbers along the Midboard pressure-port row at AoA $= 0°$. Distributions corresponding to the bottom of the fore element and those for the aft element (desaturated colors). Attachment-line (horizontal dashed line) and sonic (horizontal dash-dotted line) C_p-values.

$2.125°$. Admittedly, the Midboard row was plagued by several transient turbulent wedges for the corresponding Run #208 ($M = 0.8$), see Fig. 13. Nevertheless, the transition region still appears to be correctly extrapolated at the higher angles of attack; see Fig. 13(b). Under these conditions ($M = 0.8$, high AoA), the entire chord of the fore element is supersonic and the transition region is accompanied by what appear to be Mach or shock waves emanating from the root of the wing.

5. Conclusion

This article evaluated the laminar flow achieved on the suction side of the fore element of the S207 slotted, natural-laminar-flow (SNLF) wing at full-scale transonic conditions in the NASA Ames 11-Foot Transonic Wind Tunnel (11-FT TWT) facility. Although measurement data are available for the pressure side, the present article focuses on the suction side of the fore element.

Two technical contributions were implemented toward this end. The first is a post-processing methodology for extracting the laminar-to-turbulent transition-region location from infrared (IR) thermography video data. The methodology employs systematic masking of unavoidable measurement artifacts, and a Hough transform to fit the upstream and downstream extents of the transition region on a frame-by-frame basis, approximating the spanwise-averaged intermittency region between the onset of transition and breakdown, and to quantify its temporal uncertainty. The second is the application of an established stability analysis pipeline to the obtained experimental data. The pipeline feeds the measured C_p-distributions into the compressible boundary-layer solver DEKAF to reconstruct the laminar base flow, and solves the Linear Parabolized Stability Equations (LPSE) with EPIC to compute Tollmien-Schlichting (TS) N-factor envelopes that are compared directly against the IR-measured transition locations.

At the reference condition of $M = 0.7$ and $Re_c = 13 \times 10^6$ (based on the leading-edge-orthogonal chord), laminar flow is achieved over practically the entire suction side of the fore element for angles of attack between $-1°$ and $0°$. The transition region is conservatively bounded from below by $N = 4$–5 for this particular facility. Notably, the N-factor at which the transition region occurs increases as the transition front moves upstream with increasing angle of attack; this trend, observable to a lesser extent also in the original results of Van Ingen [12, Fig. 9.19] and [11, Fig. 9], is not immediately obvious and deserves a deeper investigation in future work. Furthermore, the N-factor isocontours become nearly vertical in the x/c–AoA plane in the rooftop region of the fore element, reflecting an inflection point in the pressure gradient there, rendering it increasingly more favorable for $x/c \gtrsim 40\%$. The

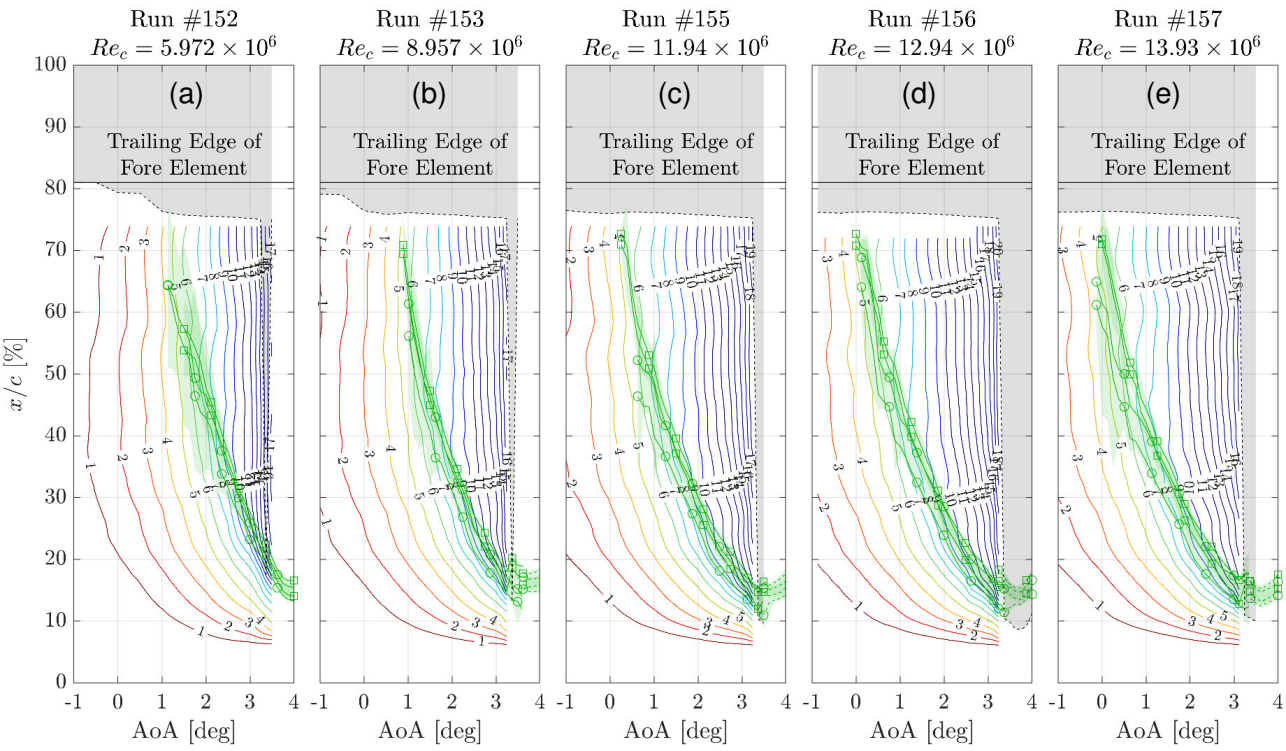


Figure 10 – Comparison of the location of transition region (symbols connected by solid lines; patch: uncertainty in time, $\pm 2\sigma$) against LPSE N-factor isocontours (colored lines) for varying Re_c along the Midboard pressure-port row on the top (suction) side: $M = 0.7$ ($\max \Delta\text{AoA} = 0.5°$ for N-factors). Locations of shock wave (symbols connected by dashed lines) and incipient separation as detected by DEKAF (dashed black line).

near-vertical isocontours imply a high sensitivity of the transition location to small changes in angle of attack when the critical N-factor is reached. As the Reynolds number is decreased, the stronger favorable pressure gradient arising from the thickened boundary-layer displacement thickness stabilizes the TS instability, extending laminar flow to higher angles of attack. As the Mach number is increased, both the inherent compressible stabilization of the TS mechanism and the more favorable pressure gradient extend the laminar flow region further. Together, these results demonstrate that the SNLF technology achieves its design intent across a broad range of transonic cruise conditions, representing the capstone experimental demonstration of the overarching NASA University Leadership Initiative (ULI) project.

6. Acknowledgements

The authors acknowledge the Ames research staff for helping make the design a reality. In particular, the contributions of Alan L'Esperance, Ted Garbeff, and Jennifer Baerny at NASA Ames Research Center in conducting the wind-tunnel experiment and clarifying the contents of the measurement data files are gratefully acknowledged. KJG, NJP, and HLR acknowledge Ethan S. Beyak and Jay M. Patel, members of the Computational Stability & Transition Lab at Texas A&M University during the experiment, for their help in tailoring DEKAF and EPIC for the specific needs of the present work. This material is based upon work supported by the National Aeronautics and Space Administration (NASA) under cooperative agreement award number NNX17AJ95A. Any opinions, findings, and conclusions or recommendations expressed in this material are those of the authors and do not necessarily reflect the views of NASA.

7. Contact Author Email Address

Mailto: kgroot@uwyo.edu

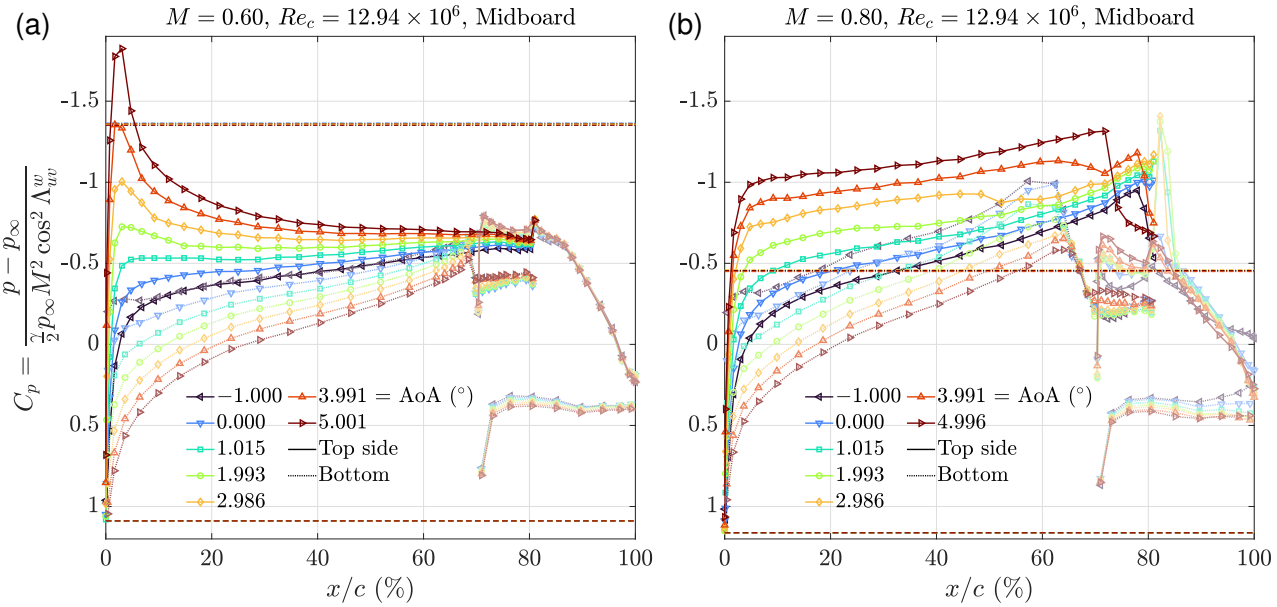


Figure 11 – Leading-edge-orthogonal C_p-distributions for a variety of angles of attack at (a) $M = 0.6$ and (b) $M = 0.8$ along the Midboard pressure-port row. Distributions corresponding to the bottom of the fore element and those for the aft element (desaturated colors). Attachment-line (horizontal dashed line) and sonic (dash-dotted line) C_p-values.

8. Copyright Statement

The authors confirm that they, and/or their company or organization, hold copyright on all of the original material included in this paper. The authors also confirm that they have obtained permission, from the copyright holder of any third party material included in this paper, to publish it as part of their paper. The authors confirm that they give permission, or have obtained permission from the copyright holder of this paper, for the publication and distribution of this paper as part of the ICAS proceedings or as individual off-prints from the proceedings.

References

[1] Joslin R D. Aircraft laminar flow control. *Annual Review of Fluid Mechanics*, 30(1):1–29, 1998.

[2] Mack L M. Boundary-layer linear stability theory. Technical Report Report No. 709, AGARD, 1984.

[3] Reed H L, Saric W S, and Arnal D. Linear stability theory applied to boundary layers. *Annual Review of Fluid Mechanics*, 28(1):389–428, 1996.

[4] Somers D M. Design of a Slotted, Natural-Laminar-Flow airfoil for a transport aircraft. Technical Report CR–2019-220403, NASA, 2019.

[5] Groot K J, Beyak E S, Heston D T, and Reed H L. Boundary-layer stability of a natural-laminar-flow airfoil at flight conditions. In *AIAA Aviation 2020 Forum*, page 3052, 2020.

[6] Heston D T, Beyak E S, Groot K J, and Reed H L. Boundary-layer stability of a slotted, natural-laminar-flow airfoil at flight conditions. In *AIAA SciTech 2021 Forum*, page 0845, 2021.

[7] Coder J G. Transonic wind-tunnel testing of a slotted, natural-laminar-flow wing at full-scale conditions. *CEAS Aeronautical Journal*, pages 1–19, 2026.

[8] Groot K J, Miró Miró F, Beyak E S, Moyes A J, Pinna F, and Reed H L. DEKAF: spectral multi-regime basic-state solver for boundary layer stability. In *2018 Fluid Dynamics Conference*, page 3380, 2018.

[9] Miró Miró F, Groot K J, Beyak E S, Moyes A J, Pinna F, and Reed H L. DEKAF: an open-source spectral boundary-layer solver. Technical report, Von Kármán Institute, Delft University of Technology, and Texas A&M University, 2020.

[10] Oliviero N B, Kocian T S, Moyes A J, and Reed H L. EPIC: NPSE analysis of hypersonic crossflow instability on yawed straight circular cone. *AIAA Paper 2015-2772*, 2015.

[11] Van Ingen J L. A suggested semi-empirical method for the calculation of the boundary layer transition region. Technical Report VTH-74, Delft University of Technology, Delft, The Netherlands, 1956.

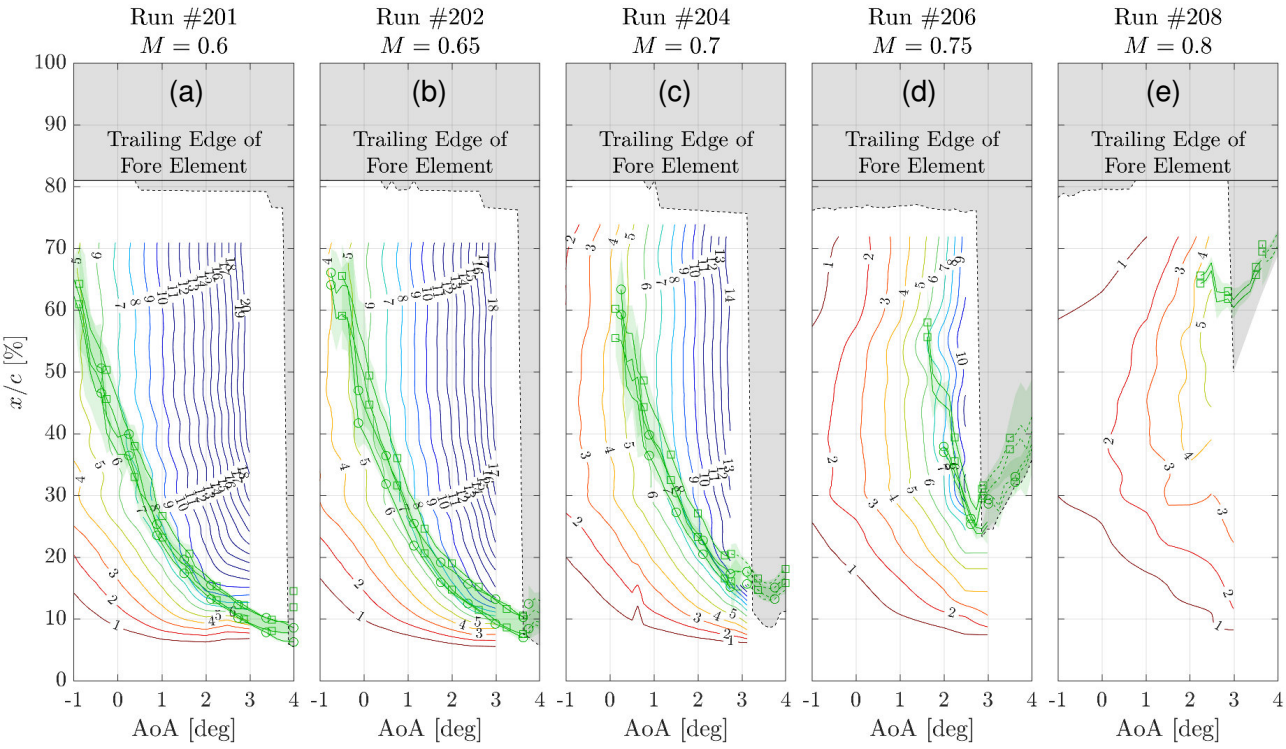


Figure 12 – Comparison of the location of transition region (symbols connected by solid lines; patch: uncertainty in time, $\pm 2\sigma$) against LPSE N-factor isocontours (colored lines) for varying M along the Midboard pressure-port row on the top (suction) side: $Re = 13 \times 10^6$ ($\max \Delta\text{AoA} = 0.5^\circ$ for N-factors). Locations of shock wave (symbols connected by dashed lines) and incipient separation as detected by DEKAF (dashed black line).

[12] Van Ingen J L. *Theoretical and experimental investigations of incompressible laminar boundary layers with and without suction*. PhD thesis, Delft University of Technology, 1956.

[13] Smith A M O and Gamberoni N. Transition, pressure gradient, and stability theory. Technical Report ES-26388, Douglas Aircraft Company, 1956.

[14] Van Ingen J L. The e^n method for transition prediction: historical review of work at TU Delft. In *38th Fluid Dynamics Conference and Exhibit*, number 2008-3830, 2008.

[15] Baals D D and Corliss W R. *Wind Tunnels of NASA*. NASA, 1981.

[16] NASA Ames Research Center. Operating Characteristics of the NASA Ames Research Center 11-By 11-Foot Transonic Wind Tunnel. NASA, link to .pdf-file, on this webpage: `https://www.nasa.gov/nasa-ames-unitary-plan-wind-tunnel/ames-unitary-plan-wind-tunnel-11-by-11-foot-twt-test-section/`, 2015. Accessed: June 14, 2026.

[17] Amaya M and Murthy S. Flow quality measurements in the NASA Ames upgraded 11-by 11-foot transonic wind tunnel. In *21st Aerodynamic Measurement Technology and Ground Testing Conference*, page 2681, 2000.

[18] Braslow A L and Knox E C. Simplified method for determination of critical height of distributed roughness particles for boundary-layer transition at Mach numbers from 0 to 5. Technical Report TN 4363, NACA, 1958.

[19] Smith A M O and Clutter D W. The smallest height of roughness capable of affecting boundary-layer transition. *Journal of the Aerospace Sciences*, 26(4):229–245, 1959.

[20] Hough P V C. Method and means for recognizing complex patterns. U.S. Patent 3,069,654, 1962.

[21] Duda R O and Hart P E. Use of the Hough transformation to detect lines and curves in pictures. *Communications of the ACM*, 15(1):11–15, 1972.

[22] Gartenberg E and Roberts A S. Airfoil transition and separation studies using an infrared imaging system. *Journal of Aircraft*, 28(4):225–230, 1991.

[23] Tropea C, Yarin A L, and Foss J F. *Springer Handbook of Experimental Fluid Mechanics*. Springer, 2007.

[24] Arnal D. Boundary layer transition: predictions based on linear theory. Technical Report R-793, AGARD,

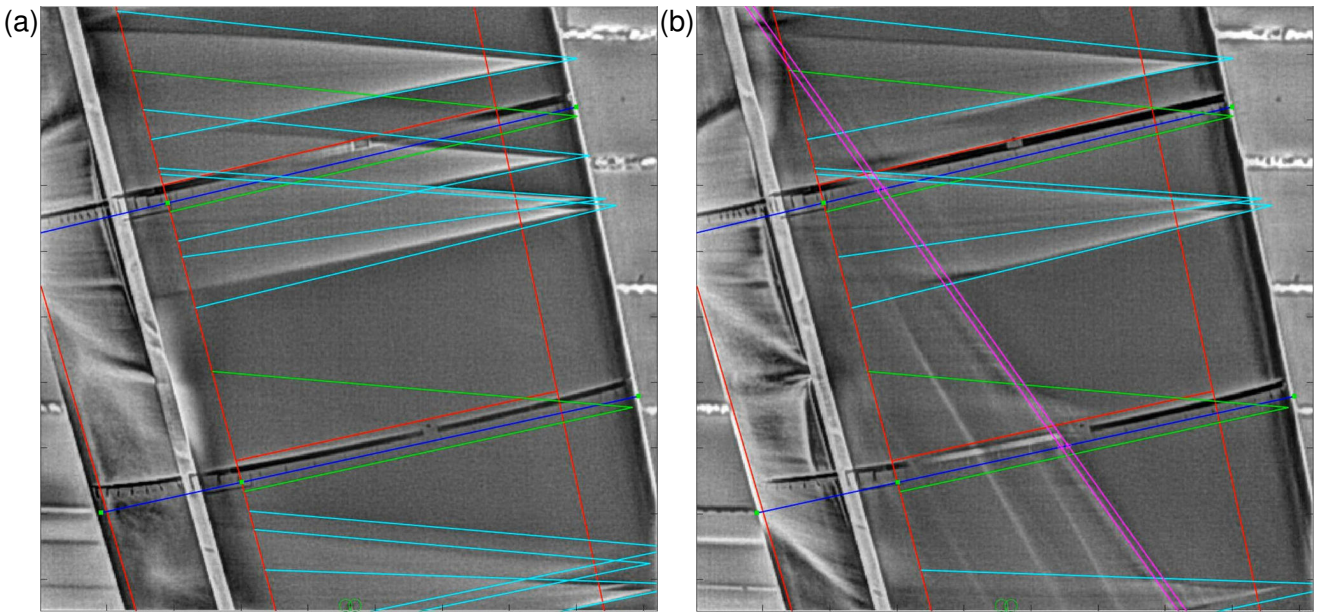


Figure 13 – Infra-red thermography frame displaying transition region (magenta lines) and masked artifacts for the In- (on top of each panel) and Midboard (bottom) pressure-tap rows during Run #208 (a,b) at AoA $= 0.249^\circ$ (a, fore element fully laminar) and 3.113° (b). Flow from right to left.

1994.

[25] George K J and Sujith R I. On Chu's disturbance energy. *Journal of Sound and Vibration*, 330(22):5280–5291, 2011.

[26] Schlichting H and Gersten K. *Boundary Layer Theory*. Springer, 8th edition, 2000.

[27] Lees L and Lin C C. Investigation of the stability of the laminar boundary layer in a compressible fluid. Technical Report TN 1115, NACA, 1946.